Circular Economy 4 (2025) 100157

Contents lists available at ScienceDirect

Circular Economy

journal homepage: www.journals.elsevier.com/circular-economy

Original Research

From construction for construction: Additive manufacturing with gas-atomized recycled steel scrap

Jan-Simeon Ludger Bernsmann *, Johannes Henrich Schleifenbaum **

Digital Additive Production, RWTH Aachen University, 52074 Aachen, Germany

ARTICLE INFO

Article history:
Received 7 February 2025
Received in revised form
27 May 2025
Accepted 23 June 2025
Available online 31 July 2025

Keywords:
Sustainability
Recycling
Steel construction
Circular economy
Additive manufacturing

ABSTRACT

Climate change and energy scarcity, as well as changing socio-demographic structures and new user needs, drive major changes in the design, construction, and operation of buildings towards sustainability. As the building sector accounts for 35% of global energy consumption and 38% of global CO_2 emissions, the energy-efficient and sustainable design and maintenance of buildings will be an effective lever for creating sustainable living conditions in the future. The use of recycled materials in construction can reduce CO_2 emissions and ensure a circu`lar economy. In this work, a proof of concept is presented for additive manufacturing by laser powder bed fusion (PBF-LB/M) of metal powder obtained by gas atomization of recycled steel from demolished buildings. From the atomization of approximately 50 kg of steel scrap, 27.8 kg of particles finer than 90 μm were obtained, whereas particles ranging between 90 μm and 315 μm accounted for 14.1 kg. The samples made from the recycled powder had a relative density of 99.9%, no porosity and excellent mechanical properties. The average tensile strength of the produced material was 808 MPa, whereas the average yield strength was 716.4 MPa. These results demonstrate the feasibility and efficiency of using gas atomized recycled steel scrap for additive manufacturing, providing high-quality materials with excellent mechanical properties suitable for construction applications.
© 2025 The Author(s). Published by Elsevier B.V. on behalf of Tsinghua University Press. This is an open access article under the CC BY license (http://creativecommons.org/licenses/by/4.0/).

1. Introduction/motivation

The European Commission's "Green Deal" targets climate change and environmental degradation by aiming to make Europe the first climate-neutral continent, emphasizing efficient resource use towards a clean, circular economy. The construction industry, which is responsible for significant global energy and CO_2 emissions, is crucial in this shift, particularly in the transition to the use of more recycled materials to reduce waste and emissions. Construction works hold vast amounts of recyclable resources, underscoring the potential of reusing building components (Churkina et al., 2020). The adoption of the EU Circular Economy Package in 2015 established clear recycling and waste-reduction targets (Broadbent, 2016). At the same time, the German Resource Efficiency Program II (ProgRess II) has pursued a hands-on strategy to cut material and energy use in key industries (Daehn et al., 2017; Kühne et al., 2019). Further studies demonstrate how sectors like construction and automotive have optimized material flows through technological innovations and circular design (Reck & Graedel, 2012; Santamouris & Vasilakopoulou, 2021). Bottom line: as society moves toward closed-loop production—use—recovery—recycling systems to curb raw-material consumption and environmental impacts, it is crucial to benchmark current recycling performance and address remaining limitations—especially in steel scrap recovery, contaminant removal, and transparent reporting—to unlock further gains in recycling efficiency (Bowyer et al., 2015; Brimacombe et al., 2001; Broadbent, 2016; Paolini et al., 2019; Reck & Graedel, 2012). However, substantial challenges remain, notably pervasive copper contamination in end-of-life scrap that cannot currently be removed during melting and leads to significant metallurgical constraints (Daehn et al., 2017). Although still in its infancy, metal additive manufacturing (AM) or 3D-printing has now arrived at a scale suitable for use in construction, offering improved economy, sustainability, safety and productivity through greater automation, enhanced customization, reduced material usage and wastage; this paper reviews recent developments in structural metal

* Corresponding author.
** Corresponding author.
E-mail addresses: jan.bernsmann@dap.rwth-aachen.de (J. S. Ludger Bernsmann), johannes.henrich.schleifenbaum@dap.rwth-aachen.de (J. H. Schleifenbaum).

https://doi.org/10.1016/j.cec.2025.100157
2773-1677/© 2025 The Author(s). Published by Elsevier B.V. on behalf of Tsinghua University Press. This is an open access article under the CC BY license (http://creativecommons.org/licenses/by/4.0/).

AM—particularly directed energy deposition-arc (DED-arc) or wire-arc AM (WAAM)—including material behaviour, structural performance, optimization strategies, hybrid applications, and future outlook and its is its ability to reduce the total environmental impact (Gardner, 2023; Ghaffar et al., 2018; Haghdadi et al., 2021; Lim et al., 2012; Mrazović et al., 2018). Historically, recycling in construction has aimed to reuse materials at the material level, treating demolished structures as resource mines. Recycling is widely recognized for its substantial material savings because it decreases the demand for newly mined raw materials (Bajaj et al., 2020). Moreover, most metals can theoretically be recycled endlessly. Especially in the commercial sector, the circular economy for steel is well developed; furthermore, US Army Directive 2019-29 and DEVCOM-ARL have demonstrated a proof-of-concept for on-demand, point-of-need recycling of scrap RHA steel—gas-atomized in a mobile foundry and processed via laser powder bed fusion—yielding martensitic powders with wrought-equivalent mechanical and ballistic performance (Pepi et al., 2021).

This work presents the use of recycled steel scrap from dismantled buildings as a material for additive manufacturing (AM) with the aim of producing sustainable and energy-efficient building components. This approach aims at reducing CO_2 emissions and promoting circularity in construction. In previous publications, the atomization of stud bolts and nuts into steel powder was investigated, and a carbon footprint examination and life cycle assessment analysis of AM-parts were conducted (Brimacombe et al., 2001; Liu et al., 2018; UNEP, 2020). Gobber et al. (2024) focused on the use of steel scrap recovered by a contractor demolished from construction sites. An analysis of the current deconstruction process has been conducted to identify which construction waste can be directly recycled and processed as raw material for AM processes such as powder bed fusion of metals with a laser beam (PBF-LB/M). Structural steel and steel products originally produced throughout the century have been amassed during dismantling activities, resulting in a diverse range of steel qualities. By isolating steel waste from demolition projects, we can assess the suitability of structural steels from different time periods. The focus is on utilizing scrap materials, especially those typically accepted as losses, owing to the impracticality of economic separation, such as reinforcing steel from smaller structures. This steel is difficult to extract because it is embedded in concrete structures and often incurs a loss even with modern equipment. To improve recycling rates, hydraulic magnets are proposed to better separate steel scraps for AM. In addition to reinforcing steel, other steel scraps, such as steel beams, are potential raw materials for AM. For use in AM, some challenges must be overcome due to the variety of different steels used over time and in various installation locations within buildings and the removal of residual concrete as well as other contaminants. To ensure the reproducibility of metal powder obtained from construction scrap, it is essential to validate the material's history and its chemical and geometric properties.

Table 1
VIGA process parameters used in the study (a single atomization process).

VIGA process parameter	
Gas pressure (bar)	32
Gap setting of gas nozzle (mm)	0.6
Diameter of stone nozzle (mm)	5.7
Increased melt temperature (°C)	1540–1581
Gas consumption (Argon) (kg)	Approx. 30–35[a]

[a] Measurement accuracy results from the measurement temperatures.

In this work, scrap samples were categorized based on age, component type, and condition, followed by material testing to evaluate their suitability for subsequent AM processes. The scrap was then converted into a metal powder via gas atomization, and the mechanical properties of the material after manufacturing by PBF-LB/M were investigated. The results demonstrate that the mechanical properties and, therefore, the approach of using recycled scrap for manufacturing by PBF-LB/M are suitable for construction applications.

2. Materials and methods

2.1. Powder atomization

The materials were supplied by Paul Kamrath Ingenieurrückbau GmbH, Dortmund, Germany, and were taken from demolition projects. The samples were categorized by age (0–25 years, 25–75 years and >75 years), component type (beam, reinforcement, or cast material), and condition (painted, oxidized, bare, or adhering to contaminants such as concrete residues). The steel scrap was first chopped into smaller pieces of approximately 10–15 cm. These samples were then sandblasted to remove minerals, oxide layers, paint, and residuals from the concrete and other construction materials. Material tests were then performed, as described in Section 3.2, to determine if the samples most suitable for atomization also met the material technology requirements.

The atomization was carried out with an ALD VIGA 2B (ALD Vacuum Technologies GmbH, Hanau) using the parameters shown in Table 1. Since the capacity of the crucible allowed only a maximum of approximately 14.5 kg material per atomization, several batches were atomized and subsequently combined. The various scrap pieces were mixed and atomized depending on their ability to be stacked within the crucible since the demolition of the buildings severely deformed the reinforcing steel and T-beams, limiting the possibility of stacking the steel scrap within the available volume of the crucible (see Figs. 1(a)–1(c)). After the first atomization batch of material, the atomization process was adapted, and all subsequent atomization batches were produced via these adapted process parameters (see Table 1, right column). Initially, a significant discrepancy between the target and the actual powder size distribution (PSD) was observed. Consequently, the process parameters and their influence on part quality were systematically investigated in a separate study, which is not discussed in this work. This study involved adjusting various parameters, such as the melt temperature, gas nozzle gap, gas pressure, and nozzle stone diameter to enhance powder yield and achieve the desired PSD. Throughout these adjustments, gas heating was consistently maintained. The final parameters used for the first and all subsequent atomization methods are provided in Table 1.

Following the atomization process, the resulting metal powder was air classified to extract ultra-fine particles below 10 μm. The residual powder was sieved twice, with the first stage filtering particles above 315 μm and the second stage focusing on those above 90 μm. After these preparatory steps, the powder quality was checked via several analyses, including PSD, chemical composition assessment, and flowability analysis. Finally, the individual powder batches from each atomization process were blended into one single batch, which was sieved and subsequently analysed as described above.

2.2. Powder characterization

The PSD of the individual batches of atomized metal powder as well as the final blend was analysed via a Camsizer X2 particle size analyser (Microtrac Retsch GmbH).

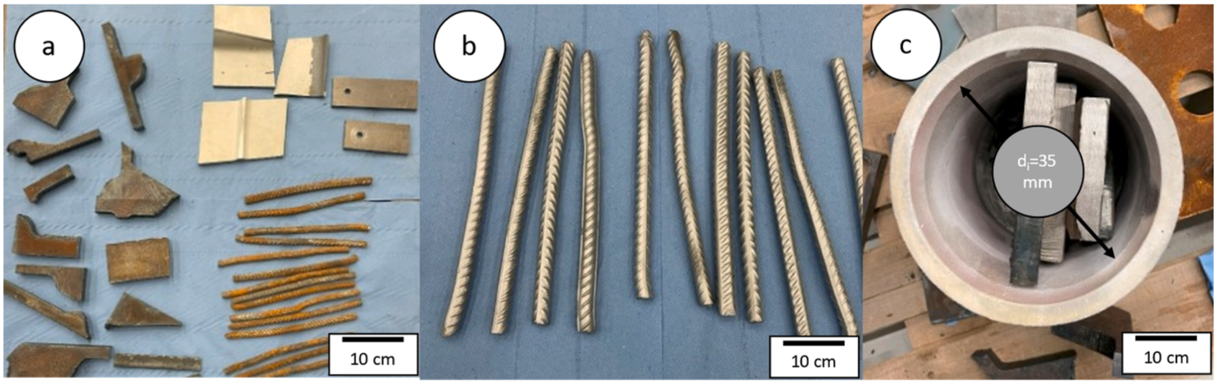

Fig. 1. (a) Examples of extracted steel scrap parts from the construction industry, such as T-beams, reinforcing steel, gusset plates and facade brackets. (b) Pieces of reinforcing steel cleaned of impurities. (c) Example of stacking individual steel scrap components inside the ceramic crucible. The displacement volume of the stopper rod for actuating the stopper in the atomization process is shown in gray.

Table 2
Process parameter levels and the resulting process window within the minima and maxima.

	Process parameter I	Process parameter II
Laser power P_L (W)	285 ± 14.25 (5%)	330 ± 16.5 (5%)
Scan speed (mm/s)	960 ± 48 (5%)	1850 ± 92.5 (5%)
Layer thickness D_s (μm)	40	40
Pre-temperature (°C)	80	80

In addition, a Phenom XL G2 desktop scanning electron microscope (SEM) was used to perform scans of powder morphology, such as circularity and elongation, using powder embedded in Bakelite. A magnifier of 310 was used with an FW of 880 μm and 10 kV HV. The detection mode of the backscattered electron detector (BSD) was "BSD-Full" of a work distance (WD) of 10.139 mm and an internal vacuum of the chamber at 60 Pa.

The flowability of the mixed and sieved powder was determined with a REVOLUTION Powder Analyser (Mercury Scientific, Inc.). The drum size used was 8 cc, and the avalanche threshold was set to 120 deg, with a rotation speed of 3 rounds per minute. The number of multiple runs was set to three. For this work, the angle of internal friction (AIF), rest angle/angle of repose, cohesion, unconfined yield strength and flow function (FF) were evaluated.

2.3. PBF-LB/M process

PBF-LB/M was carried out via an M290 (EOS GmbH, Munich, Germany) equipped with a 400 W fiber laser.

To investigate the effects of varying process parameters on the relative density and microstructure of the produced parts, a process parameter variation was conducted. The samples were fabricated with distinct sets of process parameters, including the laser power, scanning speed, and hatch spacing. The values shown in Table 2 were varied by plus and minus 5%, respectively. This variation was evenly distributed across the parameter space on a total of 100 test samples to enable a comprehensive analysis of the influencing factors.

In the following, the normalized enthalpy model is used to investigate the melting mechanism in more detail. The specific enthalpy ΔH is calculated from the parameter's laser power, scanning speed, beam diameter, and material properties such as the absorption coefficient α and thermal diffusivity a. The thermal diffusivity can be calculated from the thermal conductivity κ, density ρ, and specific heat capacity c of the material. The enthalpy at the melting point is calculated from the density ρ, specific heat capacity c, and melting temperature T_m (Forien et al., 2020; Scipioni Bertoli et al., 2017). For a given material, a set of different material properties were used: the absorption coefficient $\alpha = 0.64$, with a wavelength of 1.06 μm; the thermal diffusivity a was calculated using the thermal conductivity $\kappa = 50$ W/(mK), density $\rho = 7850$ kg/m^3 and specific heat capacity $c = 4950$ J/(kg·K), and the melting point temperature $T_m = 1813{,}15$ K of the material.

One hundred samples were fabricated with specific variations in process parameters. Among these, 55 samples were produced with a D_s of 40 μm, whereas the remaining 45 samples were

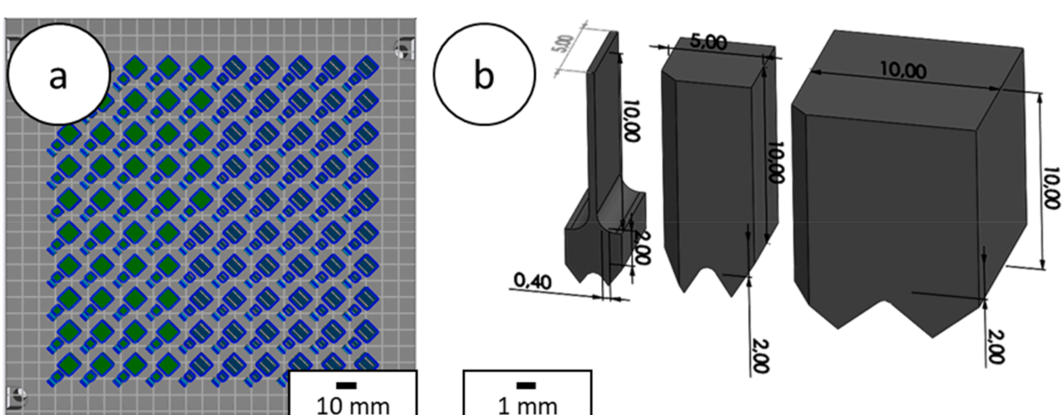

Fig. 2. (a) One hundred sample sets, each with three different test sample geometries. (b) Thin-walled test sample geometry, solid test specimen geometry with longer hatches within the geometry A = 5 mm × 5 mm, solid test specimen geometry A = 10 mm × 10 mm.

produced with a D_s of 20 μm (see Fig. 2(a)). The sample layout within the slicing software is given in Fig. 2(a), in which a single layer is shown. On the left side, the 20 μm samples are shown with their hatching vectors, whereas the right side represents the 40 μm samples. Different layer thicknesses were achieved by depositing layers of 20 μm thickness and skipping the exposure every second layer for the samples with 40 μm layer thickness. To analyse the relative density, three different sample geometries were assigned to every parameter set (see Fig. 2(b)).

To determine whether thin-walled structures could be produced, test samples with dimensions of 0.4 mm × 5 mm were used. Additionally, square test samples with dimensions of 5 mm × 5 mm and 10 mm × 10 mm were produced. This served the purpose of examining test samples with different strip lengths and volumes, which differ significantly in their expression of the incorporated heat, because the temperature evolution with increasing sample height differs, especially with limited heat conduction through the tooth-shaped support structure of the sample geometry, which was made a total of 12 mm in hight, but only the top 10 mm were considered for the analysis method.

The EOSTATE Exposure OT monitoring (optical tomography) suite was used for real-time, camera-based monitoring of the PBF-LB/M process in the EOS M 290. The system facilitates layer-by-layer mapping of components. A high-resolution industrial camera operates in the near-infrared spectrum to capture detailed data on material melting behavior throughout the entire build process. The system was used for early identification of defects within the build process of the samples in this work.

2.4. Metallography

For the microstructural analysis, samples were ground with up to 1200 grit SiC papers followed by mechanical polishing using 6- and 1-μm diamond suspensions. For light optical microscopy (LOM) imaging, the samples were etched with Lichtenegger–Bloech solution (an aqueous solution containing hydrogen difluoride and potassium metabisulfite) for 4–5 min at room temperature. For high-resolution imaging, the preparation was completed by electrolytic polishing in Struers A2 electrolyte for 15 s at 28 V, followed immediately by etching in Nital (3% nitric acid in ethanol) for 5 min.

Various SEM methods—secondary electron (SE), backscattered electron (BSE), electron channelling contrast imaging (ECCI), electron backscatter diffraction (EBSD), and energy-dispersive X-ray spectroscopy (EDS)—were performed on a Zeiss Sigma field emission gun (FEG) scanning electron microscope (SEM) with EBSD and EDS detectors by Oxford. For EBSD, a voltage of 20 kV with a working distance of 17 mm and a step size of 60 nm was chosen. EDS, BSE, and ECCI micrographs were recorded at a voltage of 15 kV with a working distance between 7 and 9 mm.

2.5. Mechanical characterization methods

The samples produced for tensile testing were machined to obtain round dog bone tensile specimens with dimensions of B6 × 20, according to DIN 50125. The build-up direction was perpendicular to the strain direction. Quasi-static uniaxial tensile tests were then performed on a Zwick/Roell (Ulm, Germany) Z4204 device at room temperature and a strain rate of $2.5 \times 10^{-4}\ s^{-1}$. For selected samples, hardness measurements were carried out in addition to the LOM recordings. The hardness measurements were conducted on a Qness 60 A + EVO hardness tester (ATM Qness GmbH, Mammelzen, Germany) in accordance with the DIN EN ISO 6507-1 standard at a test force of 0.3 kgf or ≈ 2.94 N.

2.6. Chemical characterization methods

Elemental analyses of samples, powders, and processed powders (solids) were performed via a Bruker CTX 800 X-ray fluorescence spectrometer (XRF). The measurements were repeated on three different samples in each case. In addition, via a Phenom XL G2 desktop scanning electron microscope (SEM), line scans were performed on the samples fabricated via PBF-LB/M. A magnifier of 310 was used with an FW of 1.65 mm and 10 kV HV. The detection mode was "BSD-Full" with a work distance of 10.189 mm and an internal vacuum of the chamber at 0.56 Pa.

3. Results and discussion

3.1. Powder fabrication

In our approach, we used various types of steel scraps, including reinforcement steel, residuals from gusset plate fabrication, and recycled double T carriers, to produce metal powders via the VIGA process. The individual batches of atomized metal powder representing approx. 5 kg each were blended into a single homogeneous batch after removing the fine and coarse particles by sieving. This mixing ensured uniformity in the final product with respect to the chemical composition and the PSD of the powder. Table 3 shows the chemical compositions of the selected solid steel scrap samples measured via CTX.

In Table 3, some of the chemical compositions of the selected structural steels are compared with the target composition obtained by blending the individual powders from each single atomization. The final powder composition has a high Ni value and a

Table 3
Chemical compositions of selected solid steel scrap samples, #1: beam steel avg, #2: beam steel avg, #3: reinforcement steel avg, #4: reinforcement steel avg; chemical compositions of selected standardized structural steels; chemical compositions of the mixed and produced steel powder were measured via X-ray fluorescence (XRF). All the elements are shown here except for iron, the cumulative weight percentage of which is 100%.

Sample/steel		C	Si	Mn	P	S	N	Cu	Ni
#1		—	0.16	0.74	0.02	0.02	—	0.45	0.12
#2		—	0.16	0.71	0.02	0.02	—	0.43	0.13
#3		—	0.14	1.20	0.01	—	—	0.46	0.18
#4		—	0.04	0.44	0.02	0.03	—	0.30	0.10
S235J	1.0037	0.170	–	1.400	0.035	0.035	0.012	0.550	–
S275J0	1.0044	0.210	–	1.500	0.035	0.035	0.012	0.550	–
S355JR	1.0045	0.240	0.550	1.600	0.035	0.035	0.012	0.550	–
E295	1.0050	–	–	–	0.045	0.045	–	–	–
Blended powder		–	0.222	0.835	0.016	–	–	0.093	2.347

Table 4
Particle morphology summary based on count.

Property	Average	SD	Median
Area (μm^2)	727.47	1411.9	196.84
Circle equivalent diameter (μm)	24.10	18.6	15.83
Perimeter (μm)	90.46	82.6	56.01
Circumscribed circle diameter (μm)	29.70	24.2	19.79
Convexity [1]	0.93	0.04	0.95
Circularity [1]	0.79	0.14	0.81
Elongation [1]	0.24	0.15	0.21

low Cu value compared with those of the initial scrap materials. The observed discrepancies in the powder composition compared with the scrap measurements can arise for several reasons. First, the heterogeneity of scrap metal can lead to non-uniform composition; even with comprehensive chemical analysis, the sampled area may not represent the entire bulk material, leading to variations in the final powder. This is particularly true when the surface composition differs significantly from that of the core, especially if the scarp has been exposed to varying environments or processes. Second, measurement variability, such as with XRF or CTX techniques, can yield different results depending on the measurement location, particularly for heterogeneous materials such as scrap metal, where surface oxidation or contamination might affect the readings. Finally, during the melting and atomization process in the VIGA system, certain elements may segregate or preferentially oxidize, leading to their enrichment or depletion in the final powder, as elements with a relatively high affinity for oxygen might form oxides and be lost as slag, thus altering the final composition (Bartzsch et al., 2023; Karlsson et al., 2005).

The presence of nickel (Ni) and manganese (Mn) in steel powder significantly influences its properties, especially in AM. Ni enhances toughness and ductility, particularly at low temperatures, and improves the workability of the powder, reducing the risk of cracking during processing. This is crucial for high-strength materials. Mn acts as a deoxidizer and increases the strength and hardness of steel, contributing to the structural integrity of the printed part. However, excessive Mn levels can increase susceptibility to hot cracking during solidification if not properly managed. Thus, a balanced composition of Ni and Mn is essential for achieving optimal strength, ductility, and processability, minimizing defects such as cracking or porosity (Haase & Barrales-Mora, 2019; Song et al., 2025; Zhang & Farrar, 1997).

The PSD of a metal powder, which is determined by atomization process parameters, is crucial for optimizing material usage and ensuring quality in AM processes. In applications such as PBF-LB/M, particles smaller than 10 μm and larger than 90 μm are not ideal, leading to inefficiencies and potential defects in the final product (Habibnejad-korayem et al., 2021; Haferkamp et al., 2021). Therefore, precise control of the PSD through careful optimization of atomization parameters is necessary, and post-atomization sieving is required to achieve the desired PSD, as process fluctuations can result in particles that are either too large or too small. Surface analysis of the powder embedded in Bakelite revealed mostly spherical particles with no porosity or inclusions, as detailed in Table 4. The particle morphology summary is based on count as average, standard deviation (SD) and median. Approximately 50 kg of steel scrap underwent atomization, yielding 27.8 kg of particles finer than 90 μm, 14.1 kg of particles between 90 μm and 315 μm, and 1.8 kg of particles larger than 315 μm. Additionally, 3.1 kg of the output comprised flakes rather than spherical particles, indicating variations in the atomization process (Lüdecke et al., 2024). Fig. 3 shows the frequency distribution q3(x) of the particle sizes as a bar chart. It shows the proportion of particles with a fixed particle size (each in μm). Most particles are approximately 5–40 μm in size. The distribution based on the number in p3(x) is also shown. Within the batch, more than 50% (d50) of the particles are smaller than 39.5 μm, and more than 90% (d90) are smaller than 77.5 μm (see Fig. 3). The volume-related sphericity (SPHT) was also determined. This describes how uniform the surface texture and shape of a particle are. The perfect spheres have a sphericity of 1. The relative densities and mechanical properties of the components increase with increasing sphericity of the powder used. The optimum value of sphericity is SPHT = 0.9 (Klee et al., 2022). The mean value of the sphericity of the powder used was measured at SPHT = 0.806.

In Fig. 3, q3 denotes the differential, volume-based particle size distribution, i.e., the fraction of the total particle volume contained within a narrow size interval around diameter x (subscript “3” indicates a volume basis). Correspondingly, p3 represents the percentage of the total particle volume assigned to the *i*-th size class (often reported as % rather than as a density such as % μm^{-1}). The notation x_c,min,3 refers to the lower boundary (or, if specified as x_c,3, the midpoint) of the third size class on a volume basis; exact column headings follow the instrument software convention.

The utilization of recycled materials in metal powder production through atomization presents a sustainable alternative to conventional recycling methods, aligning with the principles of closed-loop material flows and industrial symbiosis (Duflou et al., 2024; Jawahir & Bradley, 2016). Producing powders directly from industrial waste can substantially lower CO_2 emissions compared

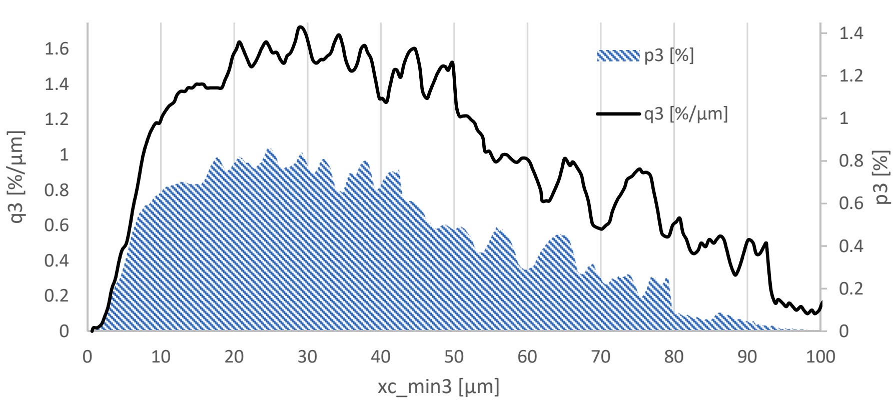

Fig. 3. PSD <90 μm of atomized steel scrap: differential, volume-based particle size distribution (q3), particle volume assigned to the size class (p3) and lower boundary of the third size class on a volume basis (xc_min3).

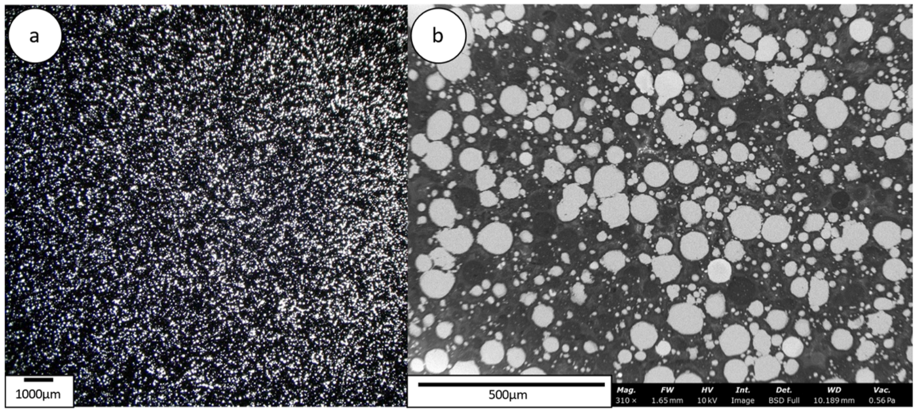

Fig. 4. Images of cross-sections of atomized, mixed steel scrap powder subjected to reflected light microscopy: (a) reflected light microscopy and (b) SEM image.

with traditional methods using primary or secondary feedstocks, as evidenced in research by Benedetti et al. (2024). For example, the average carbon footprint for the production of UNS S32760 duplex stainless steel under solution annealing conditions is 5.4 ± 5% $kgCO_2$/kg for primary production and 1.3 ± 7% $kgCO_2$/kg for secondary production. With a current recycled content of 0.37 ± 5% in wt% and applying the recycled content approach of Hammond and Jones (2011), the effective carbon footprint is approximately 3.9 ± 7% $kgCO_2$ per kg of raw material (Gobber et al., 2024). In the context of atomization processes for powder production, this baseline value significantly influences environmental impact assessments. For example, under identical gas atomization conditions, the carbon footprint for coarser powders (20–63 μm or 63–150 μm) could more than double, whereas for finer powders (<20 μm), it would increase by 15%–28% (Gobber et al., 2024). This highlights the critical environmental considerations tied to recycled material usage in powder production, even before accounting for additional impacts from pre-manufacturing or material preparation stages (Allouhi et al., 2015; Baitz et al., 2023; Gobber et al., 2024).

Microscopy images of the powder are shown in Fig. 4. The individual powder particles are mostly spherical and have no porosity, inclusions, or other defects. The numerical analysis of the evaluation is shown in Table 4.

The particles are highly spherical, with a circularity of 0.79 and an elongation of 0.24. This is typical for powders atomized by the VIGA process (Gobber et al., 2024). The average diameter of the measured particles was 24.10 μm, with a standard deviation (SD) of 18.6 μm and a median value of 15.83 μm. Not only does the particle morphology play a critical role in the properties of the powder, but other factors, such as the PSD, impurities, chemical composition, moisture content, particle density, and bulk physical properties, also significantly influence the final part quality (Cobbinah et al., 2020; Vock et al., 2019). These parameters collectively determine the powder's flowability, packing density, and overall performance during processing. The observed particle morphology, characterized by its high circularity and moderate elongation, is generally recognized as suitable for use in this process, supporting consistent behavior during spreading and melting. These characteristics are essential for achieving the desired mechanical properties and surface finish in printed components (Benedetti et al., 2024; Habibnejad-korayem et al., 2021; Haferkamp et al., 2021; Vock et al., 2019).

The results of the flowability studies are shown in Table 5. A cohesion of 0.298 kPa was measured, and the unconfined yield strength was 0.212 kPa. This results in a flow function of 5.9. As powders with FFs between 4 and 10 are considered easy to flow, the powder is suitable for use in PBF-LB/M in terms of its flowability (Lutter-Günther et al., 2017; Zegzulka et al., 2020).

Furthermore, the angle of internal friction was measured at 46.5°, and the angle of repose (AOR) was 30.7°. The concept of an ideal bulk material is defined by the internal friction angle, which is inherently linked to the angle of internal friction (Mihlbachler et al., 1998; Freeman, 2007; Zegzulka, 2003, 2013). The critical angle of repose is the steepest angle at which a granular material can be piled relative to a horizontal surface without collapsing. At this angle, the material on the slope is almost sliding. The angle of repose varies from 0° to 90°. For an ideal bulk composed of spherical particles, especially for PBF-LB/M, the angle of repose is 25°–30° (Baesso et al., 2021; Bouabbou & Vaudreuil, 2023; Jadhav et al., 2021; Zegzulka et al., 2020). Powders that have values less than 40° are considered well-flowable powders; however, the shape and texture of the material play a significant role in determining this angle; smoother and rounder grains have a lower angle of repose than rough, interlocking grains do. These characteristics suggest that metal powders nearing this ideal could be well suited for powder bed fusion processes ((Jadhav et al., 2021; Freeman, 2007). Therefore, the powder obtained here should be suitable for PBF-LB/M because its angle of repose is 30.7°.

The properties of the powder used cannot be examined in isolation. The behavior of the powder in bulk differs significantly from its performance during processing, highlighting the interdependence of these characteristics. Furthermore, the cross-correlation between various powder properties and their collective influence on the quality of the final product must be considered. This comprehensive understanding is essential for optimizing powder handling and processing techniques to achieve the desired material performance outcomes (Jadhav et al., 2021; Vock et al., 2019).

According to Zegzulka et al. (2018) powders that demonstrate good flowability for use in PBF-LB/M should have a flow function greater than 25 and an effective angle of internal friction not exceeding 35°. Powders that comply with these values are aluminum, zinc and stainless-steel powder. However, some poor-flow powders, such as copper and titanium powders, are still

Table 5
Results of flowability characterization of atomized steel scrap (Batch 1).

	Batch 1 (<90 μm)
Angle of internal friction (deg)	46.5
Rest angle/angle of repose (deg)	30.7
Cohesion (kPa)	0.29884
Unconfined yield strength (kPa)	0.2122
Flow function (–)	5.9

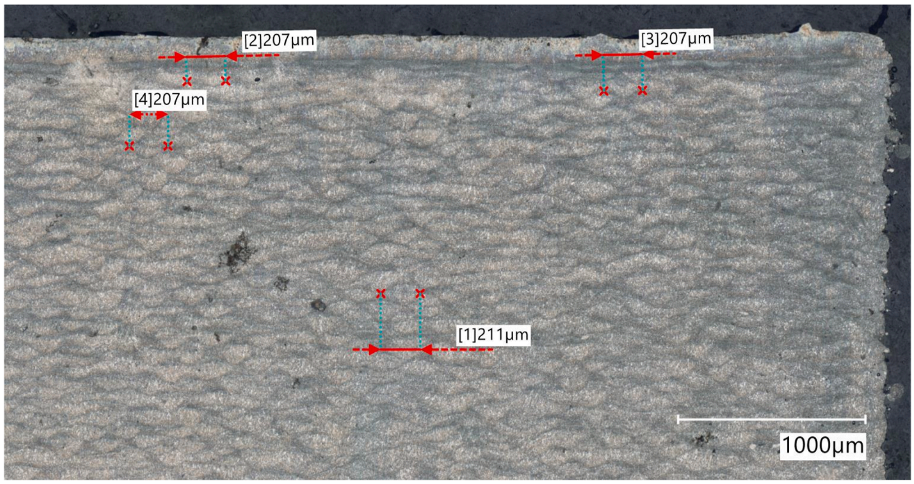

Fig. 5. Optical microscopy images of etched cross sections of samples with process parameter PP#9 (10 mm × 10 mm × 10 mm, melt pool width and track spacing, $P_L = 310$ W, $v_S = 115$, $\Delta S = 208$ µm).

successfully used in PBF-LB/M. The metal powder obtained in this work from steel scrap falls into the range of powders with lower flowability, with a flow function value of 5.9 and an effective angle of internal friction of 46.5°. This could mean a somewhat more challenging powder to work with in PBF-LB/M in terms of flowability; however, there are many more factors that may influence the final part quality (Vock et al., 2019).

3.2. PBF-LB/M

The atomized powder produced from the construction steel scrap was then used to produce samples via the PBF-LB/M process. Not all samples could be fully completed, and some were cancelled during the process to avoid jeopardizing the entire build job. Deactivation was carried out based on issues detected with the aid of process monitoring (OT). These issues were characterized in particular by strong inhomogeneities and thermal gradients in the false color image. In addition, some test samples presented defects such as delamination, pores, and highly raised edges.

The etched cross-sections overlap the melt pools in the vertical direction, which indicates a sufficiently high energy input and thus a correctly set laser power and scanning speed. In the horizontal direction, however, there is insufficient connection between neighboring melt pools, resulting in pores between the scan vectors. This can also be seen in the cross-sections of the samples with a large track spacing, in which the defects are arranged in a linear pattern (see Fig. 5).

The track spacing is determined by the weld pool width (W) and the degree of overlap (Or) between adjacent weld lines. For PP#9, $W = 208$ µm. Using reported overlap values of $Or = 0.3$ and $Or = 0.54$ (Dong et al., 2019), the optimum track spacing is calculated as $\Delta yS = 62.4$, or $\Delta yS = 112.32$ µm. The guide value of the Meiners is $\Delta yS = 0.7 \times 208$ µm $= 145.6$ µm for a focus diameter (d_S) of 78 µm (Dong et al., 2019; Meiners, 1999; Tenbrock et al., 2020). All methods yield a suitable track spacing of 65–150 µm for the given parameters. The pores in the samples produced due to lack of fusion can therefore be explained by the track spacing being set too high. It is therefore to be expected that the porosity can be reduced by a smaller track spacing. Parameter studies confirm that the melt pool width increases as the scanning speed decreases. The dependence of the melt pool width on the scanning speed is particularly pronounced at speeds below 200 mm/s (Hagedorn, 2013), but other defects, such as balling, can occur if the scanning speed is too low (Stoll, 2023).

The influences of the process parameters, the laser beam source, and other influences that can lead to differences in the study are discussed below. To assess the causes of pore formation, the existing melting mechanisms in the tests are discussed first. Although the individual scan vectors in the etchings are easily recognizable and the melt pool width can therefore be relatively clearly determined, the melt pool depth cannot be measured precisely. The reason for this is the overlap of the melt pools in the vertical direction and the partially irregular arrangement of the melt lenses, especially in the etched samples. For a clear determination of the melt lens geometry, a single exposure must be carried out under otherwise identical conditions. The melting mechanism cannot therefore be deduced from the aspect ratio of the melting lenses according to Elmer et al. (1990a, 1990b). For this reason, analytical methods from the literature are used. The model of the irradiated intensity from the field of laser beam welding only requires knowledge of the parameters of the laser beam and is therefore suitable for an initial overview. Laser powers of 270 and 346.5 W were used in the test series, and the d_S was kept constant at 78 µm. This results in irradiation intensities of 5.65×10^5 W/cm^2 and 7.25×10^5 W/cm^2, respectively. The values are within the transition range specified by Tenbrock et al. (2020), in which a change from heat conduction welding to deep penetration welding takes place.

In the following, the normalized enthalpy model is used to investigate the melting mechanism in more detail. Table 6 shows the process parameters and the resulting normalized enthalpy (H_N).

The calculated normalized enthalpy is below the limit of six to eight specified in the literature for the occurrence of deep penetration welding (Scipioni Bertoli et al., 2017). According to the model, heat conduction welding is the main melting mechanism in the tests carried out. Larger pores, which can be observed

Table 6
Process parameters and normalized enthalpies of the test series.

P_L (W)	v_s (mm/s)	d_S (µm)	H_N (−)
270	912	78	1.85
270	1942.5	78	1.27
346.5	912	78	2.38
346.5	1942.5	78	1.63

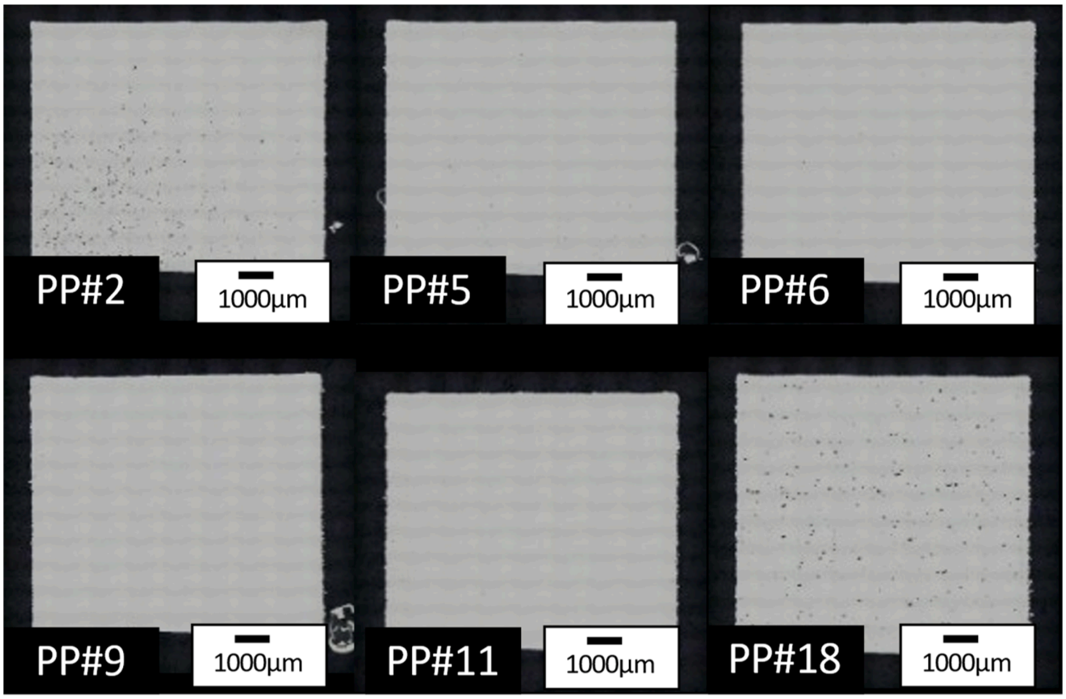

Fig. 6. Optical microscopy images of cross sections of samples (10 mm × 10 mm × 10 mm) produced by PBF-LB/M with varying process parameters (see Table 7). The four samples with the highest relative density (PP#5, PP#6, PP#9 and PP#11) and the two with the lowest relative density (PP#2 and PP#18) are shown.

Table 7
Process parameters for stable process conditions resulting in RD ≥ 99,25%.

Sample	P_L (W)	v_s (mm/s)	h_s (µm)	D_s (µm)	d_S (µm)	VED (J/mm^3)	V_{th} (mm^3/s)	RD (%)
PP#9	310	1950	115	40	78	34.559	8.97	100
PP#11	310	1950	85	40	78	46.757	6.63	100
PP#6	290	1200	65	40	78	92.948	3.12	99.98
PP#5	270	1800	75	40	78	50	5.40	99.97
PP#2	310	1350	115	40	78	49.919	6.21	99.26
PP#18	290	1500	115	40	78	42.03	6.90	99.26

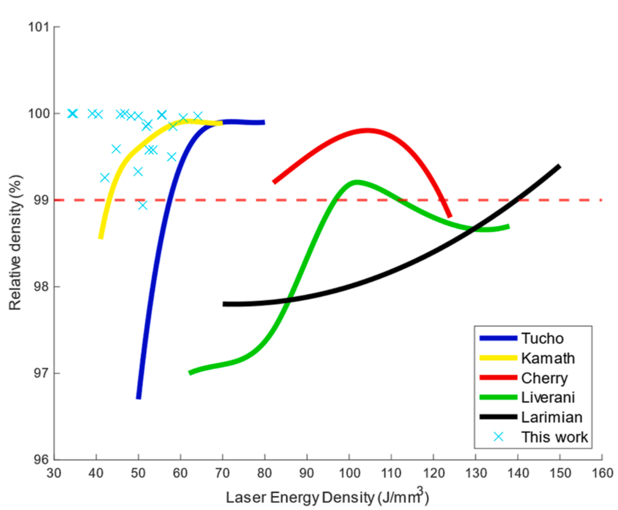

Fig. 7. Ranges of energy densities (Ahmed et al., 2022) and corresponding densification values collected from various studies for SS316L samples: Tucho (Tucho et al., 2018), Kamath (Kamath et al., 2014), Cherry (Cherry et al., 2015), Liverani (Liverani et al., 2017), and Larimian (Larimian et al., 2020).

sporadically in the samples, are therefore not due to the presence of keyholes. Instead, lack of fusion can be identified as the main cause of the pores in the cuboid samples (Elmer et al., 1990a, 1990b; Forien et al., 2020; Scipioni Bertoli et al., 2017).

Throughout the study, 24 parameter sets with relative densities greater than 99.59% were identified. A selection of six parameter sets is presented, four with high relative density and two with lower relative density. Among the four sets with high relative density, two each are shown for high and low theoretical build-up rates (see Fig. 6).

The process parameters of these sets are shown in Table 7. This work focuses on those process parameters with which a relative density (RD) greater than 99.95% was achieved under the secondary condition that the build-up rate V_{th} is maximized.

All process parameter combinations with both the highest laser power (310–320 W) and the highest scanning speed (1800–1950 mm/s) lead to non-porous (>99.9%) metallic compounds, so several process windows lead to a stable process over a wide range. A trend was observed regarding the scan distance, as non-porous specimens were always produced for scan distances ≥65 µm.

Fig. 7 illustrates the VED ranges over the part relative density within this study and furthermore collects values from various studies and their resulting densifications in the PBF-LB/M process using an SS316L alloy. The combinations of the various parameter sets mentioned above resulted in an ED ranging from 34.19 to 92.95 J/mm^3. For higher densification (above 99%), the optimum range of energy density values is scattered between 45 and 65 J/mm^3.

Even for higher energy density values, e.g., 92.95 J/mm^3, the resulting density values were greater than 99.9%. In this study, a stable process was observed over a wide range of parameter sets. For the final selection of the parameter set to produce the tensile samples for the verification of the mechanical properties, the build-up rate was further considered. Among all 100 process parameter sets, the theoretical buildup rates V_{th} varied between 1.35 and 8.97 mm^3/s.

Fig. 7 also shows that further literature values exist for the 316L alloys, which examine the structure of test samples that were manufactured with volumetric energy densities (VED) of up to 150 J/mm^3. In this work, we achieved relatively high densities of the samples despite the use of comparably low VED. This phenomenon could be attributed to the unique chemical composition of the materials employed, which significantly differs from findings from other studies (see Fig. 6) (Hearn, 2021; Zhang & Farrar, 1997). Moreover, our results highlight the interdependencies of critical parameters such as the laser power, scan speed, scan spacing, and layer thickness. Investigating these relationships is essential for assessing the reliability of VED as an optimization metric for the process, as varying parameter combinations can induce different thermal behaviors that subsequently affect the microstructure and performance of the end products. Additionally, standardization of powder properties is crucial before establishing a patterned processing window for the parts. The reliance on machine-specific powders leads to inconsistencies in the performance of the fabricated part due to varying powder characteristics, indicating that optimized process parameters may not be universally applicable across different machine models. Further investigations into these factors may provide deeper insights into enhancing material performance under diverse processing conditions.

A final process parameter set was defined to produce the subsequent tensile samples. The PBF-LB/M processes of samples PP#9, PP#11 and PP#16 were characterized by stable melting baths, low thermal gradients and a smooth process. However, process parameter set 9 had the highest theoretical build-up rate of 8.97 mm^3/s. As this can offer a decisive advantage regarding the component sizes commonly used within the construction industry, parameter set 9 was therefore chosen for the production of the samples for tensile testing.

Table 8 provides a summary of the process parameters for achieving high densification of SS316L in the process, which were compiled from various literature sources. The table also includes a comparison of these parameters with those used in this study, highlighting key similarities and differences.

The table summarizes the process parameters from various studies on achieving high densification of SS316L because there is no reported literature that indicates the use of the same alloy with PBF-LB/M and compares them to the current work (PP#9 and PP#11). While the literature reports a wide range of laser powers (100–400 W), scan speeds (125–1900 mm/s), and layer thicknesses (20–250 µm), the parameters used in PP#9 and PP#11–310 W power, 1950 mm/s scan speed, and 85 µm layer thickness—are notable for achieving a 100% relative density, surpassing reported values, which typically range between 99.18% and 99.9%. Despite the use of relatively low energy densities (34.559 J/mm^3 for PP#9 and 46.757 J/mm^3 for PP#11), both parameter sets achieve optimal densification, highlighting their efficiency. This contrasts with the literature, where higher energy densities are often required for similar results. Additionally, the

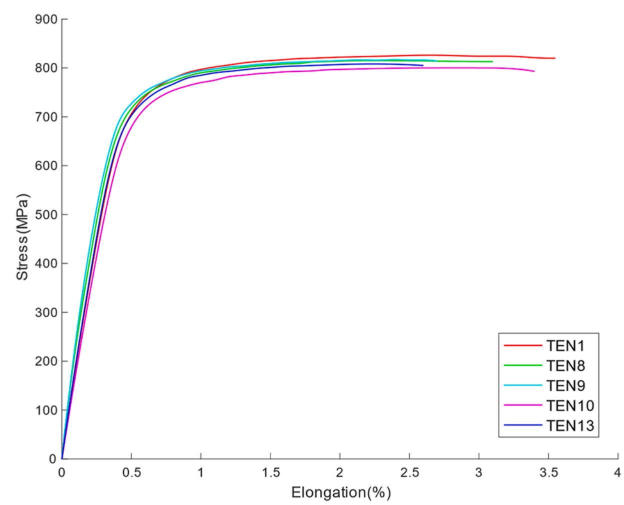

Fig. 8. Results of the tensile tests of samples produced by PBF-LB/M with process parameter set 9.

Table 8
Summary of the process parameters collected from the literature for high densification of SS316L in the PBF-LB/M process. "'—" indicates the information not reported in the literature according to Ahmed et al. (2022) and the comparison to this work.

Reference	P_L (W)	v_s (mm/s)	h_s (µm)	D_s (µm)	d_s (µm)	VED (J/mm^3)	PSD (µm)	RD (%)
Tucho et al. (2018)	150	781	80	30	–	80	–	99.86
Yakout et al. (2019)	250	800	100	40	–	78	75	98
Kamath et al. (2014)	400	1900	105	30	54	67	–	99.5
Cherry et al. (2015)	180	400	124	50	70	104.5	15–45	99.62
Liverani et al. (2017)	150	700	70	20	50	153	–	99.9
Choi et al. (2016)	380	2000	35	50	80	109	–	99.87
Shi et al. (2020)	400	125	240	250	70	53	5–41	99.99
Wang et al. (2012)	150	300	60	35	70	238	25	98.5
Salman et al. (2019)	175	668	120	30	–	73	36	99.9
Yusuf et al. (2017)	200	1600	–	50	–	–	15–40	99.18
Yasa and Kruth (2011)	85	200	144	30	180	98	–	99.9
Król et al. (2018)	125	480	10	50	35	174	15–45	99.95
Kurzynowski et al. (2018)	200	220	–	50	200	–	20–63	99.8
Choi et al. (2016)	100	800	80	25	110	58.4	10–45	99.2
PP#9 (This work)	310	1950	115	40	78	34.6	10–90	100
PP#11 (This work)	310	1950	85	40	78	46.8	10–90	100

Table 9
Mechanical properties obtained for PP#9 in this work and for various reference unalloyed, general structural steels according to CEN (2019).

Name	Number	R_e (MPa)	R_m (MPa)	A_{80} (%)
S235J	1.0037	235	360–510	26
S275J0	1.0044	275	430–560	13
S355JR	1.0045	355	510–680	12
E295	1.0050	295	490–660	10
Specimen (PP#9)	–	716.4 ± 17.2	808.6 ± 6.9	2.60 ± 0.29

PSD of 10–90 μm used here is broader than what is typically reported, yet densification remains uncompromised. A significant challenge in comparing results lies in the lack of consistent data across studies, as many studies fail to report crucial parameters such as energy density, powder size, or layer thickness. Furthermore, variations in chemical composition and powder characteristics (e.g., particle size distribution and purity) make direct comparisons difficult. The findings from PP#9 and PP#11 demonstrate the effectiveness of carefully optimized process parameters for achieving superior results in the process. Tensile samples were produced via parameter set PP#9, with their axis parallel to the build-up direction due to the low amount of powder available (Hearn, 2021).

3.3. Mechanical characterization

Tensile tests were then carried out on the produced samples (Fig. 8). On average, a tensile strength of 808 ± 6.9 MPa was achieved with this material. The average yield strength was determined to be 716.4 ± 17.2 MPa. The highest and lowest values for the mechanical parameters within the study were determined as follows: for tensile strength, a minimum of 800.4 MPa and a maximum of 826.4 MPa were achieved.

The lowest yield strength was 684.26 MPa, and the highest yield strength was 747.28 MPa. One graph with the lowest (TEN13), two with the highest results (TEN1 & TEN10) and one representative test representing the average mechanical parameters (TEN8) within the study are shown. Table 9 shows the average values for several conventionally manufactured construction steels and their mechanical properties, such as yield strength (R_e), tensile strength (R_m) and elongation at break (A_{80}), for comparison.

In terms of yield strength, a doubling of the mechanical properties was achieved with the powder mixture compared with the 1.0045 structural steel. The tensile strength achieved was 18% better than that of 1.0045. This advantage arises from the ability of the PBF-LB/M process to produce fine microstructures and high-density components with minimal defects. The rapid cooling rates in PBF-LB/M contribute to finer grain sizes, enhancing the strength and hardness. The material evaluated in this study exhibited notable differences in mechanical properties compared with those of standard steels. While the new steel demonstrated superior yield strength and tensile strength, it exhibited a significant trade-off in terms of ductility, characterized by considerably lower elongation at break. This reduced elongation at break is particularly critical in construction applications, where the ability to withstand deformation prior to failure is crucial for safety and predictability. The increased strength of the new steel comes at the cost of increased brittleness, potentially limiting its suitability for certain structural applications. In a post-heat treatment of the produced steel, a controlled tempering process could enhance the ductility and elongation of the material at break by allowing the relaxation of internal stresses. This process refined the microstructure, leading to a more uniform and stable phase distribution. As a result, the elongation of the treated steel increased at break, indicating a transition toward more ductile behavior, making it more suitable for applications requiring increased flexibility and toughness.

This effect is further elucidated through detailed analysis of the tensile samples, specifically by examining the mode of failure and the fracture surfaces. The brittleness of the new steel is evidenced by a distinct brittle fracture pattern, which contrasts with the more ductile failure observed in standard steels. Fracture surface analysis provides insights into the microstructural factors contributing to these differences, highlighting the trade-offs between increased strength and reduced ductility in the new mixed chemical composition steel. The fracture surfaces of the tensile samples were analysed, as displayed in Fig. 8. All the fracture surfaces presented *trans*-granular dimple-like and intergranular fracture areas. The intergranular failure of the samples indicates weakening of the grain boundaries (Lynch, 2019). A reason for this could be that the underlaying microstructure of low-alloy carbon steel at ambient temperature can consist of pearlite, bainite, or martensite, depending on the cooling rate, which is known for PBF-LB/M to be higher than 10^7 K/s for austenitic steel (Eskandari Sabzi & Rivera-Díaz-del-Castillo, 2020; Hooper, 2018; Kosiba et al., 2023). The transformations to bainite and pearlite are competitive and result in stable phases. Once a portion of steel transforms into either pearlite or bainite, further transformation into other microstructures is not possible without reheating to form austenite. Martensite, on the other hand, forms when austenite is rapidly cooled (quenched) to a sufficiently low temperature, preventing carbon diffusion and inhibiting the formation of pearlite or bainite. Unlike pearlite and bainite, martensite is not an equilibrium phase because the quenching process traps carbon within the austenitic structure. When heated above approximately 250 °C, martensite tends to transform into other structures as carbon begins to diffuse within the lattice (Bhadeshia & Honeycombe, 2006). The mechanical behavior of low-carbon steel microstructures varies significantly. Martensite is the hardest and strongest but also the most brittle, making it unsuitable for most structural applications. However, heat treatment between 250 °C and 650 °C produces tempered martensite, which improves ductility and formability without significantly reducing strength. This improvement is due to the transformation of martensite into stable ferrite and cementite phases, which begin at temperatures above approximately 300 °C (Bhadeshia & Honeycombe, 2006; Shaheen et al., 2020). The relatively low elongation at fracture and the lack of necking at the fracture point indicate a brittle nature at fracture of the samples (see Fig. 9) (Kirby, 1995; Shaheen et al., 2020).

A targeted thermomechanical refinement protocol could mitigate the pronounced loss of ductility observed in the atomized material while preserving its superior tensile and yield strengths. Specifically, implementing a normalization treatment—heating the powder consolidated steel above Ac_3 (~900–930 °C) and permitting controlled air cooling—would foster the homogenization of the as-atomized dendritic microstructure and relieve intrinsic quench stresses. This could be followed by a tempering cycle at 550–650 °C to precipitate fine, uniformly distributed ferritic and pearlitic phases, thereby increasing the impact toughness and plastic deformation capacity. Alternatively, subcritical annealing just below A_1 (~723 °C) for several hours would promote recovery and recrystallization in the ferritic matrix, reducing the dislocation density and improving the formability without substantially diminishing the strength. Integrating these well-established heat-treatment routes, which are routinely applied to conventional structural steels, would likely broaden the material's performance envelope for load-bearing applications in civil engineering.

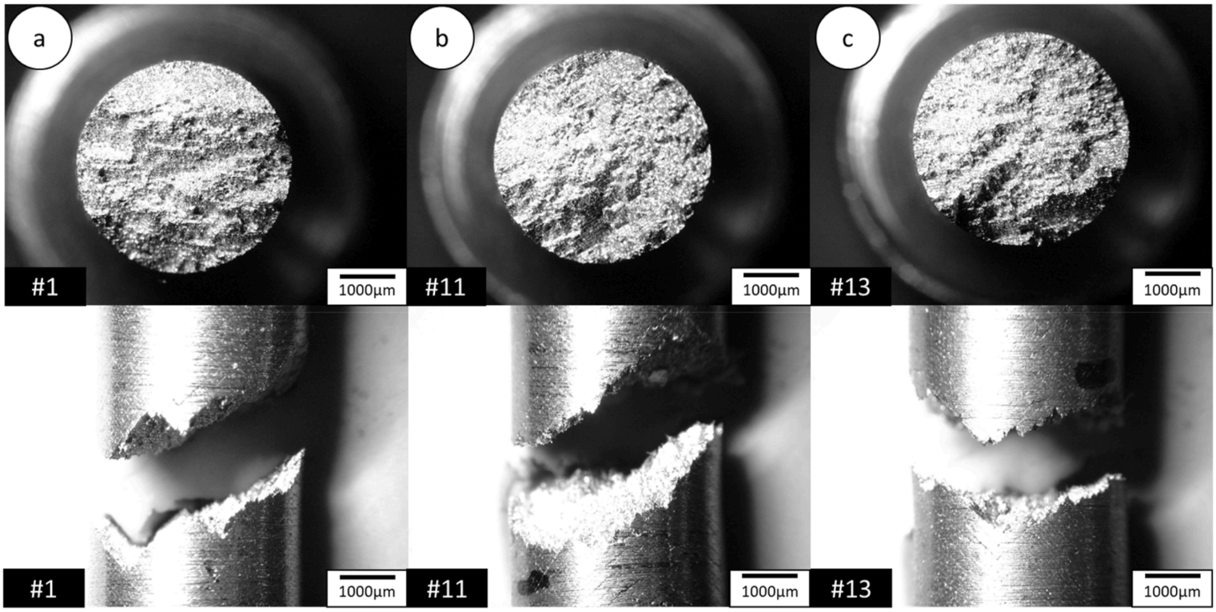

Fig. 9. Images of the fracture surfaces of three tested tensile samples: tensile sample No. 1, which had the highest yield strength and tensile strength within the study; No. 11, which was representative of the average performance of the mechanical properties; and No. 13, which was representative of the lowest characteristic values within the study. Intergranular fracture surfaces can be identified.

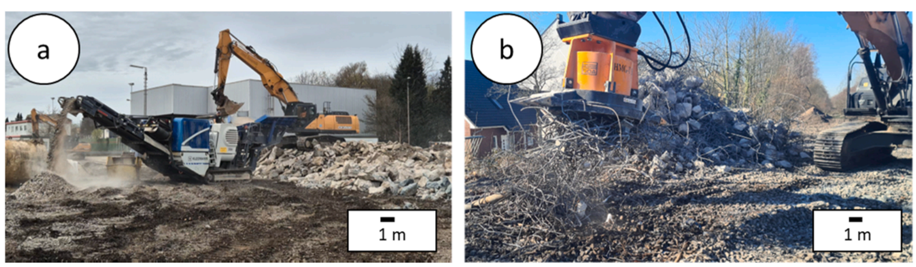

Fig. 10. (a) Processing of concrete rubble in a recycling plant. (b) Collection of steel scraps collected with a hydraulic magnet.

3.4. *Life cycle assessment*

To extract the steel scrap from the demolished concrete, the components must be heavily crushed. The recovery of reinforcing steel from demolished concrete takes place in two steps.

In the first step, the concrete demolition materials must be pulverized to reduce the particle size and separate the reinforcing steel from other materials. This process is carried out with a hydraulic excavator equipped with a pulverizer as an attachment. The aim is to crush the demolished concrete to an edge length of approx. 40 cm so that it can then be recycled. During pulverization, reinforcing steel up to a diameter of 20 mm can be separated from the concrete. The throughput rate is approximately 2–4 m^3/h, depending on the machine size. A 25-tonne excavator with an output of 133.4 kW was used. The degree of steel in reinforced concrete is typically assumed to be approx. 75 kg/m^3. Assuming that 75% can be separated during pulverization, this results in between 112.5 and 225 kg of steel per hour that can be recovered. Assuming a fuel consumption of 0.18 kg fuel/kWh according to BGL 2020 (Bauprofessor, 2021), this results in a consumption of 23.35 kg/h, which is equivalent to 0.1–0.2 kg fuel per kg steel. In the second step, the pre-treated concrete rubble is processed in a recycling plant into RC gravel with a grain size of 0–45 mm (grading curve 0/45), as shown in Fig. 10(a). Magnetic separators are used to separate additional reinforcing steel from the material (see Fig. 10(b)). After this process, approximately 95% of the original reinforcing steel is separated. Seventy-five percent of the steel is recovered from the pulverization process, approximately 5% is lost, and the remaining 20% is separated in the recycling plant.

The recycling plant processes concrete with a capacity of approx. 100 m^3/h. This corresponds to a steel recovery rate of 1500 kg/h. The combined fuel consumption for operating the excavator and the recycling plant is approximately 46.69 kg/h, which corresponds to a consumption of 0.03 kg of fuel per kg of steel. Together with the consumption from the pulverization process of steel, this results in a total consumption of 0.135–0.239 kg of fuel per kilogram of recovered steel. If this is combined with the data set “Diesel mix at refinery” from the Sphera database, the result is 0.04–0.06 kg CO_2-equivalent per kg steel.

By using extracted steel scrap for powder atomization, the production of a steel ingot can be avoided. The GWP is very low, even if the processes of cleaning and cutting to the size of the ceramic crucible have not been considered. Assuming that this steel ingot would have been produced via the blast furnace route, 1 kg of steel would cause 2.922 kg CO_2-eq. (OEKOBAUDAT, 2023b); in the electric arc furnace route, 1.459 kg CO_2-eq. (OEKOBAUDAT, 2023a). Powder atomization, in which the extracted steel is atomized into a powder for the LBPF process, is a very energy-intensive process (see Section 2.1). To evaluate this effort, the energy required for powder atomization of the 17–4 PH stainless steel powder process was taken from the literature (OEKOBAUDAT, 2023a). The energy requirement is 78–97 MJ/kg (Liu et al., 2018). Combining this energy requirement with the Sphera database on the electricity grid mix results in a GWP of 12.2–15.0 kg CO_2-eq/kg steel powder.

The share of atomization in the GWP is dominant. This is partly due to the high energy intensity but also to the proportion of fossil fuels in the German electricity mix. A larger share of renewable energy in the electricity mix in the future will significantly reduce the global warming potential in the future.

4. Conclusions

This study successfully demonstrated the feasibility of using recycled and atomized steel scrap sourced from construction demolition as feedstock for AM via the PBF-LB/M process. The produced alloy powder exhibited favourable characteristics, such as an appropriate PSD and sufficient flowability for the PBF-LB/M process.

The experimental results revealed that the samples fabricated from the recycled powder had no porosity and possessed remarkable mechanical properties, with tensile strengths surpassing those of standard structural steels. This indicates the viability of employing such materials in construction applications, where mechanical performance is paramount. Additionally, the study highlighted the importance of optimizing process parameters to achieve the desired material properties and maintain process stability.

In conclusion, guaranteeing a uniform chemical composition across individual atomization runs is challenging because of both the limited crucible capacity of approximately 14.5 kg per melt and the irregular geometry of the demolition-derived scrap. As detailed in Section 2, the atomization was carried out with an ALD VIGA 2B (ALD Vacuum Technologies GmbH, Hanau), using the parameters shown in Table 1. Since the capacity of the crucible allowed only a maximum of approximately 14.5 kg material per atomization, several batches were atomized and subsequently combined. The various scrap pieces were mixed and atomized depending on their ability to be stacked within the crucible since the demolition of the buildings severely deformed the reinforcing steel and T-beams, limiting the possibility of stacking the steel scrap within the available volume of the crucible. After the first atomization batch of material, the atomization process was adapted, and all subsequent atomization batches were produced via these adapted process parameters (see Table 1, right column). Consequently, each powder “shot” exhibited slight compositional shifts. Although this investigation was conducted at the laboratory scale, where individual powder batches remain discrete, an industrial-scale operation would naturally blend multiple atomization outputs into larger powder lots. Even so, one should anticipate that such large-scale powder blending would still reflect underlying compositional heterogeneity, with a corresponding increase in the variability of mechanical properties across the final material. In addition to optimizing separation technology, close collaboration with local scrap dealers is essential to proactively minimize fluctuations in scrap composition. Over time, material and component passports gain importance: by comprehensively recording the origin, chemical composition, and installation location, one can assess recyclability and selectively channel particle streams to meet tight specifications. This approach will make it increasingly feasible to constrain alloy variations and thereby sustainably improve the reproducibility of processed powder feedstocks. Overall, the findings provide a proof of concept for integrating recycled materials into AM techniques, offering a sustainable pathway for producing construction components. Future work will focus on further refining the separation and atomization processes, as well as scaling up production to assess the long-term durability and economic viability of this sustainable approach.

Although the laboratory-scale atomization of demolition-derived steel scrap delivers exceptional tensile and yield strengths, the pronounced deficit in ductility highlights the necessity for post-processing strategies. Conventional heat-treatment regimens—such as normalization above Ac_3 with controlled air cooling, tempering at 550–650 °C, or subcritical annealing near A_1—offer promising routes to refine the microstructure and restore plasticity. To better gauge the method's viability for real-world applications, specific future research directions must be clearly defined: (1) pilot-scale atomization campaigns to validate process consistency and powder uniformity; (2) systematic exploration of additional thermal cycles on consolidated samples to optimize the strength–ductility balance; and (3) field trials in structural components to assess in situ performance under service-relevant loading and environmental conditions. Such targeted investigations will be critical for translating the demonstrated laboratory benefits into scalable, construction-grade materials.

Despite the relatively high value of scrap metal, significant quantities still end up in landfills, e.g., the U.S. Environmental Protection Agency stated that 29% of nonferrous metals and 54% of ferrous metals are discarded rather than properly recycled (APEAL, 2022; EPA, 2021; 2024a; 2024b). Nevertheless, the environmental benefits of recycling metals are clear. Compared with the production of goods from virgin materials, the recycling of metals dramatically reduces greenhouse gas emissions by requiring much less energy—saving up to 95% of the energy for aluminum, 75% for copper, and 60% for steel (OECD, 2023; Salas, 2025; Smith & Bryant, 1975). Additionally, scrap metal recycling plays a vital role in conserving natural resources. These findings emphasize the critical need to improve metal recycling rates and recovery practices to maximize environmental and economic benefits.

By leveraging interdisciplinary engineering and innovative manufacturing technologies, this research paves the way for more sustainable construction practices, aligns with global environmental goals and contributes to a greener future. The approach not only addresses the critical issues of waste management and resource efficiency in the construction industry but also contributes to the reduction of CO_2 emissions, supporting the transition towards a circular economy.

CRediT authorship contribution statement

Jan-Simeon Ludger Bernsmann: Writing – review & editing, Writing – original draft, Visualization, Validation, Supervision, Software, Resources, Project administration, Methodology, Investigation, Formal analysis, Data curation, Conceptualization. **Johannes Henrich Schleifenbaum:** Writing – review & editing, Project administration, Funding acquisition.

Declaration of competing interest

The authors declare that they have no known competing financial interests or personal relationships that could have appeared to influence the work reported in this paper.

Acknowledgements

All of the results in this paper come from the project “Additive Manufacturing von 3D-Verbindungselementen im Bauwesen”, AddMamBa for short. This project is funded by the German Federal Ministry for Economic Affairs and Climate Action through the grant AddMamBa, FKZ 03LB3019B.

References

Ahmed, N., Barsoum, I., Haidemenopoulos, G., & Al-Rub, R. A. (2022). Process parameter selection and optimization of laser powder bed fusion for 316L stainless steel: A review. *Journal of Manufacturing Processes, 75*, 415–434.

Allouhi, A., El Fouih, Y., Kousksou, T., Jamil, A., Zeraouli, Y., & Mourad, Y. (2015). Energy consumption and efficiency in buildings: Current status and future trends. *Journal of Cleaner Production, 109*, 118–130.

APEAL. (2022). *Why steel recycles forever: How to collect, sort and recycle steel for packaging*. Available at: The Association of European Producers of Steel for Packaging (APEAL) https://circulareconomy.europa.eu/platform/en/knowledge/why-steel-recycles-forever-how-collect-sort-and-recycle-steel-packaging-0.

Baesso, I., Karl, D., Spitzer, A., Gurlo, A., Günster, J., & Zocca, A. (2021). Characterization of powder flow behavior for additive manufacturing. *Additive Manufacturing, 47*, Article 102250.

Baitz, M., Becker, T., Wolf, M., Colodel, C., Schulz, S., Coen, D., Suzaly, N., Spykman, R., Schulte, R., Hallmann, A., et al. (2023). 24 years intersectoral LCA database development, growth, and update: From PE/Thinkstep-GaBi to Sphera-MLC. *Journal of Life Cycle Assessment, Japan, 19*(4), 227–236.

Bajaj, P., Hariharan, A., Kini, A., Kürnsteiner, P., Raabe, D., & Jägle, E. A. (2020). Steels in additive manufacturing: A review of their microstructure and properties. *Materials Science and Engineering: A, 772*, Article 138633.

Bartzsch, G., Scherbring, S., Richter, J., Vollmer, M., Mola, J., Niendorf, T., & Volkova, O. (2023). Gas atomization of Al-steels. *Materials Today Communications, 34*, Article 105388.

Bauprofessor. (2021). *Betriebsstoffverbrauch von Baumaschinen (Fuel consumption of construction machinery)*. Available at: https://www.bauprofessor.de/betriebsstoffverbrauch-baumaschinen/ (in Germany).

Benedetti, M., Perini, M., Vanazzi, M., Giorgini, A., Macoretta, G., & Menapace, C. (2024). Atomized scrap powder feedstock for sustainable inconel 718 additive manufacturing via LPBF: A study of static and fatigue properties. *Progress in Additive Manufacturing, 9*, 1843–1856.

Bhadeshia, H. K. D. H., & Honeycombe, S. R. (2006). *Steels: Microstructure and properties*. Elsevier.

Bouabbou, A., & Vaudreuil, S. (2023). Numerical modelling of SS316L powder flowability for laser powder-bed fusion. *Archives of Materials Science and Engineering, 120*, 22–29.

Bowyer, J., Bratkovich, S., Fernholz, K., Frank, M., Groot, H., Howe, J., & Pepke, E. (2015). *Understanding steel recovery and recycling rates and limitations to recycling*. Available at: Dovetail Partners Inc https://www.dovetailinc.org/report_pdfs/2015/dovetailsteelrecycling0315.pdf.

Brimacombe, L., Shonfield, P., & Buridard, M. (2001). *Sustainability and steel recycling*. SAE Technical Paper 2001-01-3766. https://doi.org/10.4271/2001-01-3766

Broadbent, C. (2016). Steel's recyclability: Demonstrating the benefits of recycling steel to achieve a circular economy. *International Journal of Life Cycle Assessment, 21*, 1658–1665.

CEN. (2019). *DIN EN 10025-2:2019: Hot rolled products of structural steels - Part 2: Technical delivery conditions for non-alloy structural steels*. Available at: European Committee for Standardization (CEN) https://www.dinmedia.de/de/norm/din-en-10025-2/300863966 (in Germany).

Cherry, J. A., Davies, H., Mehmood, S., Lavery, N., Brown, S., & Sienz, J. (2015). Investigation into the effect of process parameters on microstructural and physical properties of 316L stainless steel parts by selective laser melting. *The International Journal of Advanced Manufacturing Technology, 76*, 869–879.

Choi, J., Shin, G. H., Brochu, M., Kim, Y. J., Yang, S., Kim, K., Yang, D. Y., Lee, C. W., & Yu, J. H. (2016). Densification behavior of 316L stainless steel parts fabricated by selective laser melting by variation in laser energy density. *Materials Transactions, 57*, 1952–1959.

Churkina, G., Organschi, A., Reyer, C. P., Ruff, A., Vinke, K., Liu, Z., Reck, B. K., Graedel, T. E., & Schellnhuber, H. J. (2020). Buildings as a global carbon sink. *Nature Sustainability, 3*, 269–276.

Cobbinah, P., Nzeukou, R. A., Onawale, O. T., & Matizamhuka, W. (2020). Laser powder bed fusion of potential superalloys: A review. *Metals, 11*, 58.

Daehn, K. E., Cabrera Serrenho, A., & Allwood, J. M. (2017). How will copper contamination constrain future global steel recycling? *Environmental Science & Technology, 51*, 6599–6606.

Dong, Z., Liu, Y., Wen, W., Ge, J., & Liang, J. (2019). Effect of hatch spacing on melt pool and As-built quality during selective laser melting of stainless steel: Modeling and experimental approaches. *Materials, 12*, 50.

Duflou, J. R., Wegener, K., Tekkaya, A. E., Hauschild, M., Bleicher, F., Yan, J., & Hendrickx, B. (2024). Efficiently preserving material resources in manufacturing: Industrial symbiosis revisited. *CIRP Annals, 73*, 695–721.

Elmer, J. W., Giedt, W. H., & Eagar, T. W. (1990a). The transition from shallow to deep penetration during electron beam welding. *Welding Journal, 69*, 167s–175s.

Elmer, J. W., Giedt, W. H., & Eagar, T. W. (1990b). The transition from shallow to deep penetration during electron beam welding. *Welding Research Supplement*, 167s–176s.

EPA. (2021). *Advancing sustainable materials management: Facts and figures report*. Available at: Environmental Protection Agency (EPA) https://www.epa.gov/facts-and-figures-about-materials-waste-and-recycling/advancing-sustainable-materials-management.

EPA. (2024a). *Best practices for solid waste management: A guide for decision-makers in developing countries recycling markets, EPA 530-R-23-010*. Available at: United States Environmental Protection Agency (EPA) https://nepis.epa.gov/Exe/ZyPURL.cgi?Dockey=P101F1LX.txt.

EPA. (2024b). *European climate risk assessment: Executive summary*. Available at: https://civil-protection-knowledge-network.europa.eu/media/european-climate-risk-assessment-executive-summary.

Eskandari Sabzi, H., & Rivera-Díaz-del-Castillo, P. E. J. (2020). Composition and process parameter dependence of yield strength in laser powder bed fusion alloys. *Materials & Design, 195*, Article 109024.

Forien, J. B., Calta, N. P., DePond, P. J., Guss, G. M., Roehling, T. T., & Matthews, M. J. (2020). Detecting keyhole pore defects and monitoring process signatures during laser powder bed fusion: A correlation between *in situ* pyrometry and *ex situ* X-ray radiography. *Additive Manufacturing, 35*, Article 101336.

Freeman, R. (2007). Measuring the flow properties of consolidated, conditioned and aerated powders—A comparative study using a powder rheometer and a rotational shear cell. *Powder Technology, 174*(1–2), 25–33.

Gardner, L. (2023). Metal additive manufacturing in structural engineering—Review, advances, opportunities and outlook. *Structures, 47*, 2178–2193.

Ghaffar, S. H., Corker, J., & Fan, M. (2018). Additive manufacturing technology and its implementation in construction as an eco-innovative solution. *Automation in Construction, 93*, 1–11.

Gobber, F. S., Priarone, P. C., Pennacchio, A., & Actis Grande, M. (2024). Effect of inert gas pressure on the properties and carbon footprint of UNS S32760 powders made from waste materials by gas atomization. *Journal of Materials Research and Technology, 33*, 8814–8828.

Haase, C., & Barrales-Mora, L. A. (2019). From high-manganese steels to advanced high-entropy alloys. *Metals, 9*, 726.

Habibnejad-korayem, M., Zhang, J., & Zou, Y. (2021). Effect of particle size distribution on the flowability of plasma atomized Ti-6Al-4V powders. *Powder Technology, 392*, 536–543.

Haferkamp, L., Haudenschild, L., Spierings, A., Wegener, K., Riener, K., Ziegelmeier, S., & Leichtfried, G. J. (2021). The influence of particle shape, powder flowability, and powder layer density on part density in laser powder bed fusion. *Metals, 11*, 418.

Hagedorn, Y. C. (2013). *Additive manufacturing of high performance oxide ceramics via selective laser melting*. PhD Thesis. German. (in Germany): Rheinisch-Westfälische Technische Hochschule Aachen.

Haghdadi, N., Laleh, M., Moyle, M., & Primig, S. (2021). Additive manufacturing of steels: A review of achievements and challenges. *Journal of Materials Science, 56*, 64–107.

Hammond, G., & Jones, C. (2011). *Embodied carbon: The inventory of carbon and energy (ICE)*. Available at: https://greenbuildingencyclopaedia.uk/wp-content/uploads/2014/07/Full-BSRIA-ICE-guide.pdf.

Hearn, W. (2021). *Laser based powder bed fusion of plain carbon and low-alloy steels: Microstructure and processability*. Licentiate Thesis. Sweden: Chalmers University of Technology. Available at: https://research.chalmers.se/publication/522034/file/522034_Fulltext.pdf.

Hooper, P. A. (2018). Melt pool temperature and cooling rates in laser powder bed fusion. *Additive Manufacturing, 22*, 548–559.

Jadhav, S. D., Dhekne, P. P., Brodu, E., Van Hooreweder, B., Dadbakhsh, S., Kruth, J. P., Van Humbeeck, J., & Vanmeensel, K. (2021). Laser powder bed fusion additive manufacturing of highly conductive parts made of optically absorptive carburized $CuCr_1$ powder. *Materials & Design, 198*, Article 109369.

Jawahir, I. S., & Bradley, R. (2016). Technological elements of circular economy and the principles of 6R-based closed-loop material flow in sustainable manufacturing. *Procedia CIRP, 40*, 103–108.

Kühne, R., Feldmann, M., Citarelli, S., Reisgen, U., Sharma, R., & Oster, L. (2019). 3D printing in steel construction with the automated Wire Arc additive manufacturing. In *ce/papers, 3* (pp. 577–583).

Kamath, C., El-dasher, B., Gallegos, G. F., King, W. E., & Sisto, A. (2014). Density of additively-manufactured, 316L SS parts using laser powder-bed fusion at powers up to 400 W. *The International Journal of Advanced Manufacturing Technology, 74*, 65–78.

Karlsson, H., Nyborg, L., & Berg, S. (2005). Surface chemical analysis of prealloyed water atomised steel powder. *Powder Metallurgy, 48*, 51–58.

Kirby, B. R. (1995). The behaviour of high-strength grade 8.8 bolts in fire. *Journal of Constructional Steel Research, 33*, 3–38.

Klee, L., Bergs, T., Brimmers, J., Lantzsch, T., & Häfner, C. (2022). Pulvercharakterisierung und Parameteroptimierung zur additiven Verzahnungsfertigung mittels LPBF. *RTe Journal*, 1–18 (in Germany).

Kosiba, K., Gustmann, T., Kim, J. T., Seok, J., Jung, J., Beyer, L., Scudino, S., Giebeler, L., Han, J., & Hufenbach, J. K. (2023). Experimental cooling rates during high-power laser powder bed fusion at varying processing conditions. *Journal of Alloys and Compounds, 967*, Article 171773.

Król, M., Mazurkiewicz, J., & Żołnierczyk, S. (2018). Optimization and analysis of porosityand roughness in selective laser melting 316L parts. *Archives of Materials Science and Engineering, 1*, 5–15.

Kurzynowski, T., Gruber, K., Stopyra, W., Kuźnicka, B., & Chlebus, E. (2018). Correlation between process parameters, microstructure and properties of 316 L stainless steel processed by selective laser melting. *Materials Science and Engineering: A, 718*, 64–73.

Lüdecke, M., Kuhnhenne, M., Bernsmann, J., Schulte, J., Schleifenbaum, J. H., & Kamrath, P. (2024). *Additive manufacturing of 3D connecting elements in the building industry*. https://doi.org/10.5281/zenodo.12170802

Larimian, T., Kannan, M., Grzesiak, D., AlMangour, B., & Borkar, T. (2020). Effect of energy density and scanning strategy on densification, microstructure and mechanical properties of 316L stainless steel processed *via* selective laser melting. *Materials Science and Engineering: A, 770*, Article 138455.

Lim, S., Buswell, R. A., Le, T. T., Austin, S. A., Gibb, A. G. F., & Thorpe, T. (2012). Developments in construction-scale additive manufacturing processes. *Automation in Construction, 21*, 262–268.

Liu, Z. Y., Li, C., Fang, X. Y., & Guo, Y. B. (2018). Energy consumption in additive manufacturing of metal parts. *Procedia Manufacturing, 26*, 834–845.

Liverani, E., Toschi, S., Ceschini, L., & Fortunato, A. (2017). Effect of selective laser melting (SLM) process parameters on microstructure and mechanical properties of 316L austenitic stainless steel. *Journal of Materials Processing Technology, 249*, 255–263.

Lutter-Günther, M., Horn, M., Seidel, C., & Reinhart, G. (2017). Einfluss der Korngrößenverteilung auf Fließfähigkeit und Bauteilqualität beim Laserstrahlschmelzen. In *Proceedings of the 14th Rapid.Tech conference, Erfurt, Germany* (in Germany).

Lynch, S. (2019). A review of underlying reasons for intergranular cracking for a variety of failure modes and materials and examples of case histories. *Engineering Failure Analysis, 100*, 329–350.

Meiners, W. (1999). *Direktes selektives Laser Sintern einkomponentiger metallischer Werkstoffe*. PhD Thesis. Rheinisch-Westfälische Technische Hochschule Aachen, German (in Germany).

Mihlbachler, K., Kollmann, T., Seidel-Morgenstern, A., Tomas, J., & Guiochon, G. (1998). Measurement of the degree of internal friction of two native silica packing materials. *Journal of Chromatography A, 818*, 155–168.

Mrazović, N., Baumers, M., Hague, R., & Fischer, M. (2018). Guiding building professionals in selecting additive manufacturing technologies to produce building components. *Materials Today Communications, 15*, 199–202.

OECD. (2023). *The climate implications of government support in aluminium smelting and steelmaking*. Available at: Organisation for Economic Co-operation and Development (OECD) https://www.oecd.org/en/publications/the-climate-implications-of-government-support-in-aluminium-smelting-and-steelmaking_178ed034-en.html.

OEKOBAUDAT. (2023a). *Process Data set: Steel section*. Available at: Steel sections https://oekobaudat.de/OEKOBAU.DAT/datasetdetail/process.xhtml?lang=en&uuid=755a481d-a74b-4ba0-b417-cc26767b2d50&version=20.24.070.

OEKOBAUDAT. (2023b). *Process Data set: Galvanized steel profile (electric arc furnace route, high scrap content)*. Available at: Steel sections https://oekobaudat.de/OEKOBAU.DAT/datasetdetail/process.xhtml?lang=en&uuid=42de525f-7c48-4722-b503-6f423b39b4f4&version=20.24.070.

Paolini, A., Kollmannsberger, S., & Rank, E. (2019). Additive manufacturing in construction: A review on processes, applications, and digital planning methods. *Additive Manufacturing, 30*, Article 100894.

Pepi, M., McWilliams, B., Kudzal, A., Jian, Y., Charles, M., Eonta, C., LaTour, A., Cote, D., & Park, S. (2021). Additive manufacturing with feedstock gas atomized in a shipping container from scrap steel. *International Journal of COMADEM, 24*, 37–42.

Reck, B. K., & Graedel, T. E. (2012). Challenges in metal recycling. *Science, 337*, 690–695.

Salas, E. B. (2025). *Steel industry—Statistics & facts*. Available at: https://www.statista.com/topics/1149/steel-industry/.

Salman, O. O., Brenne, F., Niendorf, T., Eckert, J., Prashanth, K. G., He, T., & Scudino, S. (2019). Impact of the scanning strategy on the mechanical behavior of 316L steel synthesized by selective laser melting. *Journal of Manufacturing Processes, 45*, 255–261.

Santamouris, M., & Vasilakopoulou, K. (2021). Present and future energy consumption of buildings: Challenges and opportunities towards decarbonisation. *e-Prime, 2021*, Article 100002.

Scipioni Bertoli, U., Guss, G., Wu, S., Matthews, M. J., & Schoenung, J. M. (2017). *In-situ* characterization of laser-powder interaction and cooling rates through high-speed imaging of powder bed fusion additive manufacturing. *Materials & Design, 135*, 385–396.

Shaheen, M. A., Foster, A. S. J., Cunningham, L. S., & Afshan, S. (2020). Behaviour of stainless and high strength steel bolt assemblies at elevated temperatures—A review. *Fire Safety Journal, 113*, Article 102975.

Shi, W., Wang, P., Liu, Y., Hou, Y., & Han, G. (2020). Properties of 316L formed by a 400 W power laser selective laser melting with 250 μm layer thickness. *Powder Technology, 360*, 151–164.

Smith, R. J., & Bryant, R. G. (1975). Metal substitutions in carbonic anhydrase: A halide ion probe study. *Biochemical and Biophysical Research Communications, 66*, 1281–1286.

Song, S., Li, G., Wu, B., Cai, Q., & He, X. (2025). Effect of Mn content on the microstructure and corrosion resistance of duplex stainless steels fabricated by wire arc additive manufacturing. *Metals and Materials International, 31*, 1738–1753.

Stoll, T. (2023). *Laser powder bed fusion von Kupfer auf Aluminiumoxid-Keramiken. Erlangen, German*. FAU University Press (in Germany).

Tenbrock, C., Fischer, F. G., Wissenbach, K., Schleifenbaum, J. H., Wagenblast, P., Meiners, W., & Wagner, J. (2020). Influence of keyhole and conduction mode melting for top-hat shaped beam profiles in laser powder bed fusion. *Journal of Materials Processing Technology, 278*, Article 116514.

Tucho, W. M., Lysne, V. H., Austbø, H., Sjolyst-Kverneland, A., & Hansen, V. (2018). Investigation of effects of process parameters on microstructure and hardness of SLM manufactured SS316L. *Journal of Alloys and Compounds, 740*, 910–925.

UNEP. (2020). *Global status report for buildings and construction: Towards a zero-emission, efficient and resilient buildings and construction sector*. Available at: https://wedocs.unep.org/handle/20.500.11822/34572;jsessionid=207DF2220247687774FE0673E0009C80.

Vock, S., Klöden, B., Kirchner, A., Weißgärber, T., & Kieback, B. (2019). Powders for powder bed fusion: A review. *Progress in Additive Manufacturing, 4*, 383–397.

Wang, D., Yang, Y., Su, X., & Chen, Y. (2012). Study on energy input and its influences on single-track, multi-track, and multi-layer in SLM. *The International Journal of Advanced Manufacturing Technology, 58*, 1189–1199.

Yakout, M., Elbestawi, M. A., & Veldhuis, S. C. (2019). Density and mechanical properties in selective laser melting of Invar 36 and stainless steel 316L. *Journal of Materials Processing Technology, 266*, 397–420.

Yasa, E., & Kruth, J. P. (2011). Microstructural investigation of Selective laser melting 316L stainless steel parts exposed to laser re-melting. *Procedia Engineering, 19*, 389–395.

Yusuf, S., Chen, Y., Boardman, R., Yang, S., & Gao, N. (2017). Investigation on porosity and microhardness of 316L stainless steel fabricated by selective laser melting. *Metals, 7*, 64.

Zegzulka, J. (2003). Granular states of material aggregation - A comparison of ideal bulk material with ideal fluid and ideal solid matter. *Bulk Solids Handling, 23*, 162–167.

Zegzulka, J. (2013). The angle of internal friction as a measure of work loss in granular material flow. *Powder Technology, 233*, 347–353.

Zegzulka, J., Gelnar, D., Jezerska, L., Prokes, R., & Rozbroj, J. (2020). Characterization and flowability methods for metal powders. *Scientific Reports, 10*, Article 21004.

Zegzulka, J., Gelnar, D., Jezerska, L., Ramirez-Gomez, A., Necas, J., & Rozbroj, J. (2018). Internal friction angle of metal powders. *Metals, 8*, 255.

Zhang, Z., & Farrar, R. A. (1997). Influence of Mn and Ni on the microstructure and toughness of C-Mn-Ni weld metals. *Welding Journal, 76*, 183.